Supplementary Information

Highly efficient H_2 production from H_2S via a robust graphene encapsulating metal catalyst

Mo Zhang,[a,b,‡] Jing Guan,[c,‡] Yunchuan Tu,[a,b] Shiming Chen,[b] Yong Wang,[a,b] Suheng Wang,[a,b] Liang Yu,[b] Chao Ma,[d] Dehui Deng[a,b,*] and Xinhe Bao[b]

[a]State Key Laboratory of Physical Chemistry of Solid Surfaces, Collaborative Innovation Center of Chemistry for Energy Materials (*i*ChEM), College of Chemistry and Chemical Engineering, Xiamen University, Xiamen 361005, China.

[b]State Key Laboratory of Catalysis, *i*ChEM, Dalian Institute of Chemical Physics, Chinese Academy of Sciences, Zhongshan Road 457, Dalian 116023, China.

[c]School of Environmental & Municipal Engineering, Qingdao University of Technology, Qingdao 266033, China.

[d]Center for High Resolution Electron Microscopy, College of Materials Science and Engineering, Hunan University, Changsha 410082, China.

[‡]These authors contributed equally to this work.

E-mail: dhdeng@dicp.ac.cn

Experimental section

Synthesis of materials

The CoNi@NGs was prepared through a template-assisted method. Briefly, 3.6 mmol $Co(NO_3)_3 \cdot 6H_2O$, 3.6 mmol $Ni(CH_3COO)_2 \cdot 4H_2O$, 1.8 g urea, 240 mg citric acid and 1.8 g 70 nm SiO_2 were added into 100 mL pure water. After heating the solution at 100 ^oC with reflux for 12 h, the precursor $CoNi(OH)_x$-SiO_2 was obtained via a centrifugal separating. Then the $CoNi(OH)_x$-SiO_2 was transferred into a CVD furnace, with temperature programmed from room temperature to 600 ^oC under 3/7 H_2/Ar, followed by bubbling CH_3CN with 80 mL/min Ar for 20 minutes at 600 ^oC. Finally, the samples were treated in 4% HF aqueous solution at room temperature for 12 h, followed by washing in distilled water and ethanol, and then drying at 60 ^oC. Co@NGs and Ni@NGs were prepared from the precursors of $Co(NO_3)_3.6H_2O$ and $Ni(CH_3COO)_2 \cdot 4H_2O$, respectively. The synthesis process of $CoNi(OH)_x$-CNTs was similar as $CoNi(OH)_x$-SiO_2 but with the CNTs to replace the SiO_2 templates during the preparation. The $CoNiO_x$-CNTs was prepared via heating the $CoNi(OH)_x$-CNTs at 400 ^oC under Ar for 1 h. The N-Carbon was prepared via destroying the graphene shells on the metal cores, oxidizing the CoNi to metal oxides at 300 ^oC with 20% O_2/Ar for 4 h and further removing the metal oxides with the acid wash (1 M H_2SO_4 and 2 M HCl) at 90 ^oC for 12 h.

Materials characterization

TEM was conducted on Tecnai F20 Transmission Electron Microscope operated at an accelerating voltage of 200 kV. HAADF-STEM and EDX mapping were carried out on the JEOL ARM200 operated at 200 kV. XAFS was measured at the BL14W1 beamline of Shanghai Synchrotron Radiation Facility (SSRF). UV-Vis test was measured from 800 nm to 200 nm on UV 2550 and UV 1900 produced by Shimadzu. XRD measurements were conducted on a Rigaku Ultima IV diffractometer with Cu Kα radiation at 40 kV and 30 mA. XPS was carried out on a Thermo ESCALAB Xi spectroscope used Al Kα X-rays as the excitation source with a voltage of 15 kV and power of 150 W. Inductively coupled plasma atomic emission spectroscopy was carried out in IRIS Intrepid II XSP. Elemental analysis test was conducted on Vario EL III produced by Elementar Analysensyetem GmbH, Germany. Faradaic efficiency was measured on gas chromatography GC 2060 produced by Ruimin Instrument Company in Shanghai.

Electrochemical measurements

All the electrochemical measurements were carried out with CHI 760E using a standard three-electrode cell equipped with a gas flow controlling system at 25 ^{o}C. The Hg/HgO reference electrode was calibrated according to the formula $E_{versus\ RHE} = 0.098 + 0.0591$ pH. pH was tested by the pH value meter at 25 ^{o}C. Three parallel tests showed that the pH of electrolyte is 12.17, so the $E_{versus\ RHE} = 0.817$ V. The test condition of oxygen evolution reaction polarization curve was similar to SOR, except for using 1 M NaOH as the electrolyte. As the pH in 1 M NaOH is 14, so the $E_{versus\ RHE} = 0.925$ V. More details can be found in the Supplemental Information.

Sulfur oxidation reaction (SOR) polarization curves

In the SOR polarization curve test, a commercial glassy carbon electrode (GCE) (5 nm in diameter) covered by the sample with Nafion ionomer as a binder was used as the working electrode. Typically, 5 mg catalyst was dispersed in 1.95 mL ethanol with 50 uL Nafion solution to form a homogeneous ink. Then 25 uL of the ink was added dropwise onto the surface of GCE by using a micropipette and dried under the room temperature. The final loading for all catalysts including comparison samples on GCE was 0.32 mg/cm^2. The activities of different samples were evaluated by rotating disk electrode (RDE) measurements with a scan rate of 2 mV/s.

Chronoamperometry test

In the chronoamperometry test, a Ni foam electrode (1 cm^2 square, 1.5 mm thickness) covered by 7 mg/cm^2 catalyst was used as the working electrode. The chronoamperometry test was carried in a double-cell electrolytic tank segregated with Nafion 117 membrane, in the one side setting working electrode and reference electrode in Ar-saturated 1 M NaOH and 1 M Na_2S electrolyte, and in the other side setting counter electrode in 1 M NaOH electrolyte. The measuring potential was 0.317 V (versus RHE) for more than 500 h. In order to weaken the influence of reactant concentration for catalyst activity, the electrolyte was replaced every 36 hours.

The rate of H_2 evolution test

The rate of H_2 evolution test was evaluated by gas chromatography with galvanostatic test at 100 mA/cm^2. During the galvanostatic test, pure Ar was purged continuously through the mass flow meter at a rate of 60 mL/min and directly routed into gas chromatography every 10 min. Quantification of the H_2 were performed using the thermal conductivity detector (TCD). The quantity and retention time of the gas were calibrated with a series of standard gas samples, which are calculated from gas chromatography chromatogram peak areas at different time in points as follow:

$$R_{H_2} = \frac{A_{test}}{A_{standard}} \times c_{standard} \times R_{Ar}$$

R_{H_2} : gas flow rate of H_2

A_{test} : peak area of the H_2 generated at the specific time point on the TCD

$A_{standard}$: peak area of the H_2 in the standard gas samples

$c_{standard}$: volume concentration of H_2 in the standard gas samples

R_{Ar} : gas flow rate of Ar

Calculation of the Faradaic efficiency

The Faradaic efficiency of H_2 are calculated from gas chromatography chromatogram peak areas at different time in points as follow:

$$i_{H_2} = R_{H_2} \times \frac{2Fp_0}{RT}$$

$$FE_{H_2} = \frac{i_{H_2}}{i_{total}} \times 100\%$$

i_{H_2} : partial current density for H_2

F : Faradaic constant, 96485 C mol^{-1}

p_0 : pressure

R : ideal gas constant, 8.314 J mol^{-1} K^{-1}

T : temperature, 298 K

FE_{H_2} : Faradaic efficiency of H_2

i_{total} : total current density, 100 mA cm^{-2}

In-situ electrochemical UV-Vis test

The in-situ electrochemical UV-Vis system was constructed by uniting the electrochemistry test system with the UV-Vis spectrophotometry test system. The electrolyte during the reaction was continuously pumped into the colorimetric dish and circulating returned to the electrolytic cell by the push of peristaltic pump, accompanying with the UV-Vis test synchronously. The change of electrolyte was monitored by this in-situ electrochemical UV-Vis system.

Recycle of oxidation product S powder

The concentrated sulfuric acid was added dropwise into the electrolyte solution until adjusting the pH to 1 in the ice bath, and then yellow product was obtained by a centrifugal separating.

DFT calculation method

All calculations were performed using the Vienna Ab-initio Simulation Package(VASP)[1-4] with the projector augmented wave method[5, 6] and a cut off energy of 400 eV. The Perdew-Burke-Ernzerh of (PBE) functional[7] for the exchange-correlation term was used with the dispersion correction developed by Grimme et al. The model of CoNi encapsulated in one graphene layer consisted of C_{240} encapsulating a $Co_{28}Ni_{27}$ cluster. To investigate the effect of nitrogen doping, the graphene doped with the graphitic nitrogen was used as the calculated model. All structures were fully relaxed to the ground state and the spin-polarization was considered in all calculations. The convergence of energy and forces were set to 1×10^{-4} eV and 0.05 eV/Å, respectively. The free energies of the intermediates were obtained by $\Delta G(S^*) = \Delta E(S^*) + \Delta ZPE - T\Delta S$, where $\Delta E(S^*)$ was the binding energy of S species, ΔZPE and ΔS were the zero point energy change and entropy change of adsorption S, respectively.

Selective removal of H_2S from industrial syngas by CoNi@NGs

The constructed configuration was similar as the configuration of chronoamperometry test mentioned above, but the electrolyte was changed to 1 M NaOH in the both cells. Before the LSV test, gases were flowed into the work cell for 2 h respectively with the flow rate of 10 mL/min to accumulate enough reaction species. Before the galvanostatic test, 2% H_2S / Syngas was also flowed into the work cell for 2 h with the flow rate of 10 mL/min to initiate the reaction. After starting the galvanostatic test at 20 mA/cm^2 current density, the flow rate of syngas was adjusted to 3 mL/min to supplement the quantity of consumed H_2S, which maintained the concentration of S^{2-} unchanged. To decrease the influence of electrolyte to reference electrode, the electrolyte was replaced in every 50 h.

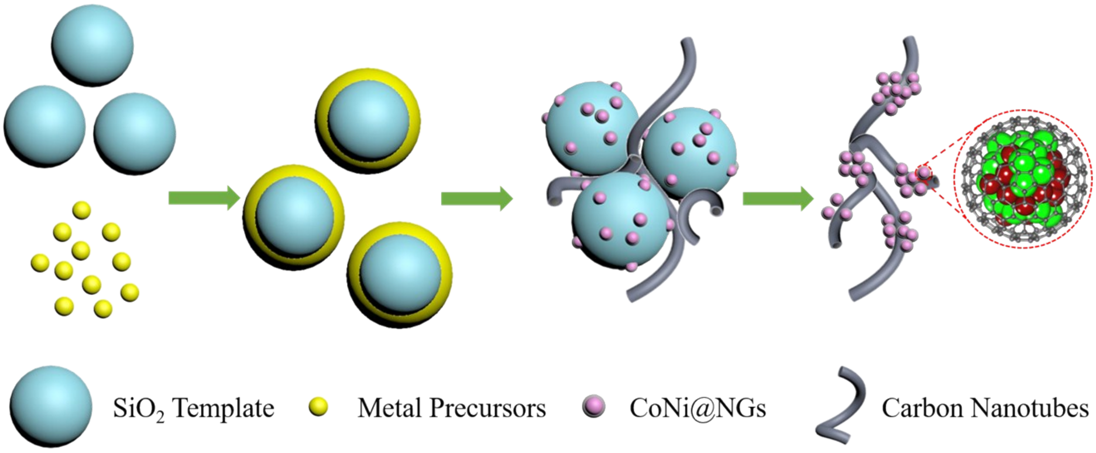

Fig. S1 Schematic illustration of the synthesis process of CoNi@NGs.

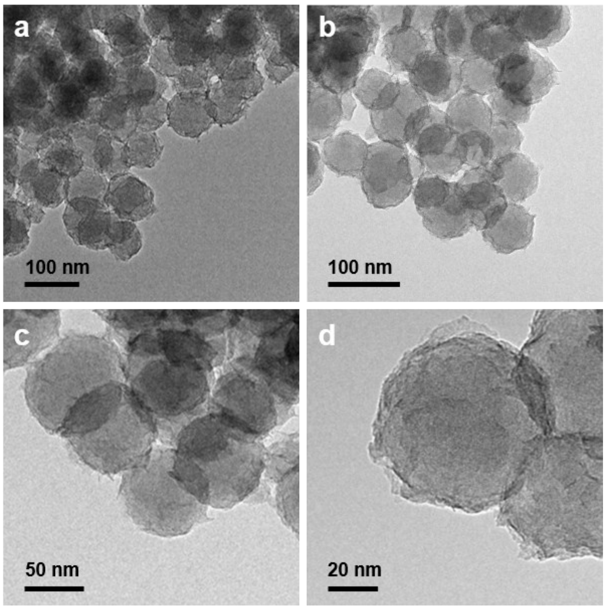

Fig. S2 TEM images of CoNi(OH)$_x$-SiO$_2$

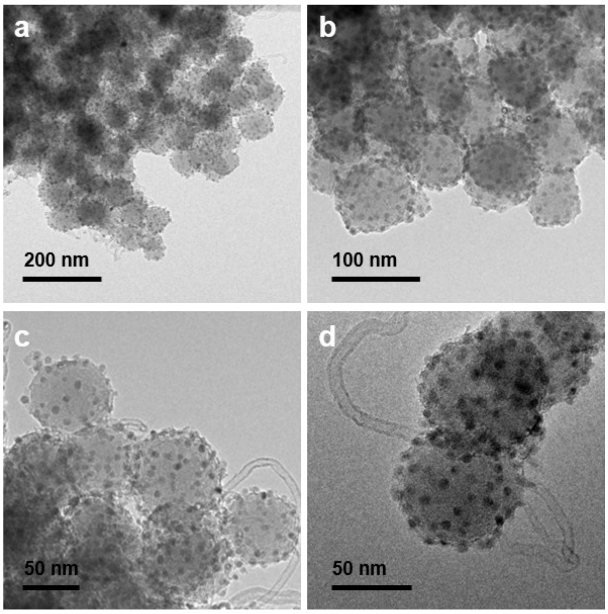

Fig. S3 TEM images of CoNi@NGs-SiO_2

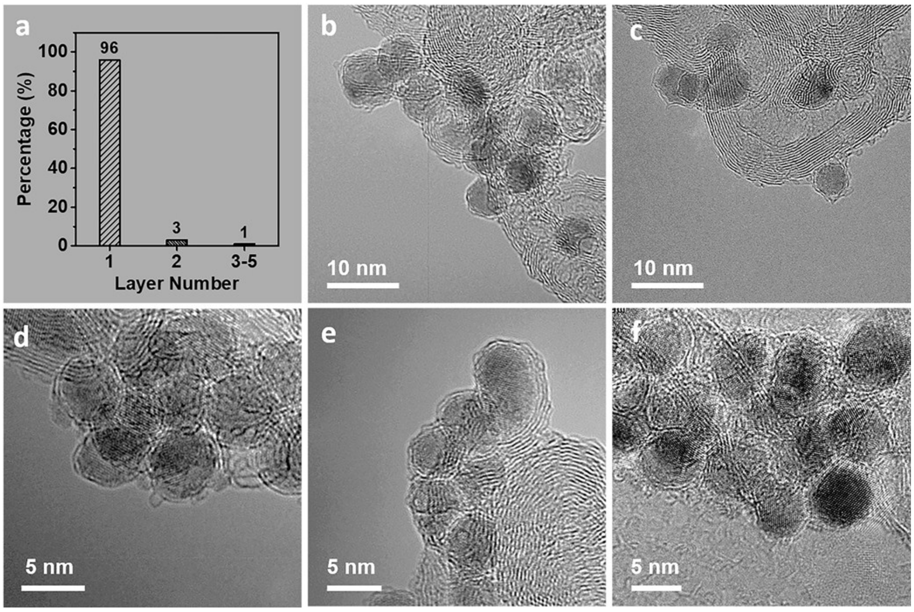

Fig. S4 The statistical analysis of the layer number of the graphene shell on metal nanoparticles. According to the statistical analysis by HRTEM images, the graphene shells on the CoNi NPs are very thin (only 1-3 layers), and most of the graphene shells (>96%) consist of only one layer.

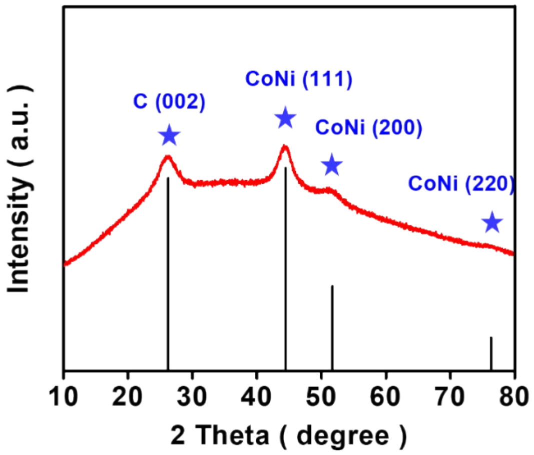

Fig. S5 XRD pattern of CoNi@NGs. The crystal structure of CoNi alloy NPs is confirmed by X-ray diffraction (XRD) test, which exhibits two main diffraction peaks at 2θ = 44.44°, and 51.72°, corresponding to the (111) and (200) facets of the CoNi alloy, respectively.

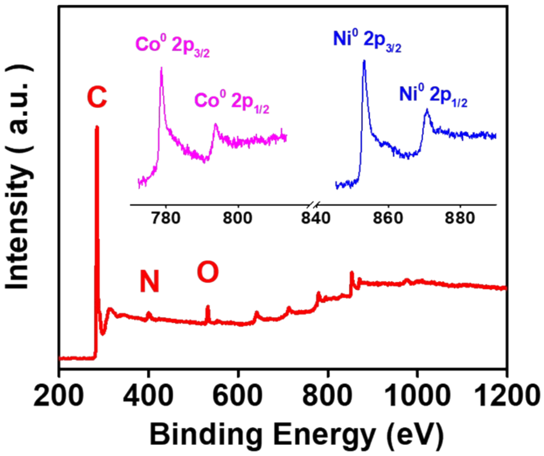

Fig. S6 Co 2p and Ni 2p XPS spectra of CoNi@NGs sample. X-ray photoelectron spectroscopy (XPS) was performed to reflect the surface chemical state of the CoNi alloy NPs. Peaks at 778.68 eV and 793.58 eV can be attributed to the Co 2p of metallic Co^0, and 853.08 eV and 870.68 eV in the Ni 2p spectrum can be assigned to Ni^0, which suggest that both Co and Ni in CoNi@NGs maintain their metallic state.

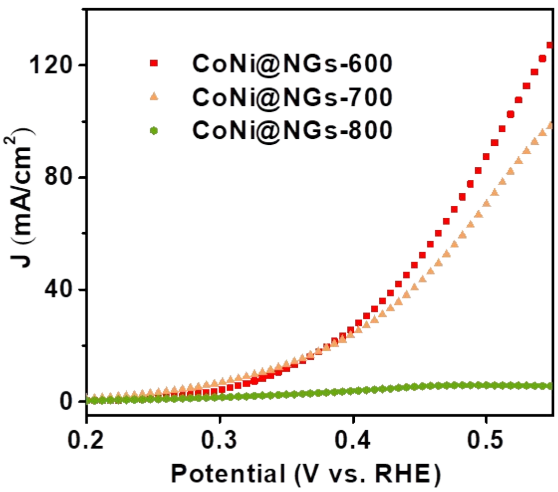

Fig. S7 Sulfur oxidation reaction (SOR) polarization curves for CoNi@NGs catalysts with different annealing temperature 600 °C, 700 °C, 800 °C. CoNi@NGs-T (T = 600, 700, 800 °C) were prepared in a similar process but use different temperatures for the graphene encapsulating. The CoNi@NGs prepared at 600 °C showed the best SOR activity compared with the higher annealing temperatures. Elemental analysis test (Table S2) indicates that N-dopants content becomes higher at lower annealing temperature, which may be one important factor to influence the activity of CoNi@NGs.

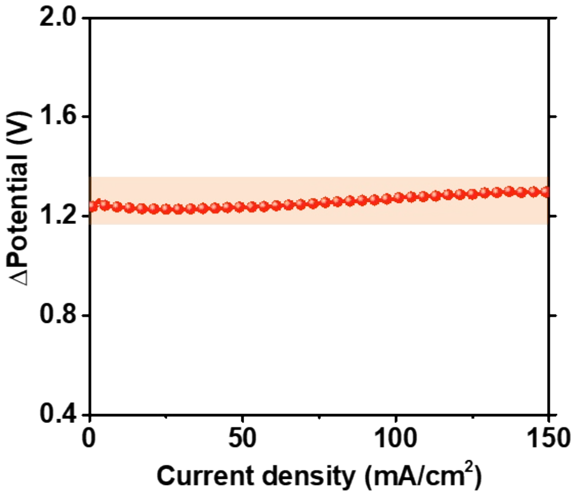

Fig. S8 The potential comparison of SOR and OER at different current density from 1-

150 mA/cm^2. The value difference of potential maintains among 1.2-1.3 V.

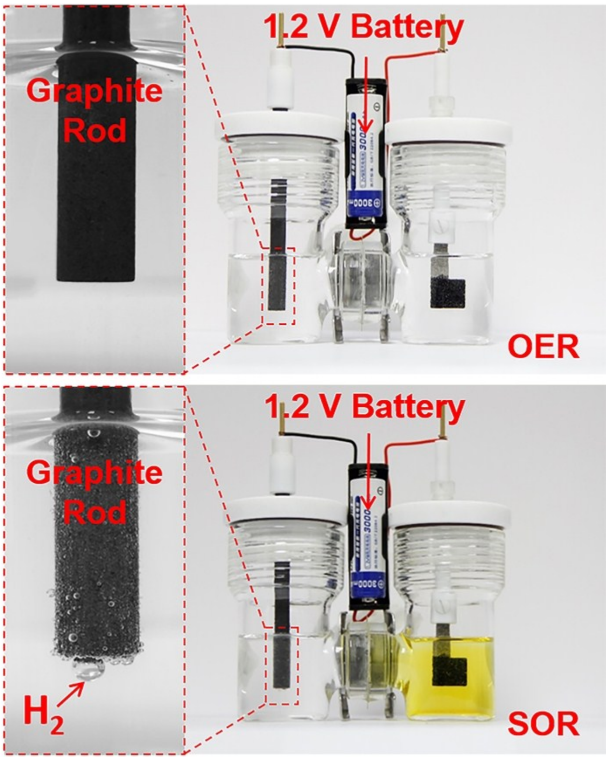

Fig. S9 The photos of devices for 1.2 V commercial battery driving splitting of H_2O (up) and H_2S (down). The enlargements in red block diagrams show the image of graphite rods. It clearly shows that no bubble producing on the graphite rod in the up picture, which means splitting of water can not be driven by 1.2 V commercial battery. In contrast, there are abundant bubbles producing on the graphite rod in the down picture, which means 1.2 V battery can easily drive the decomposition of H_2S.

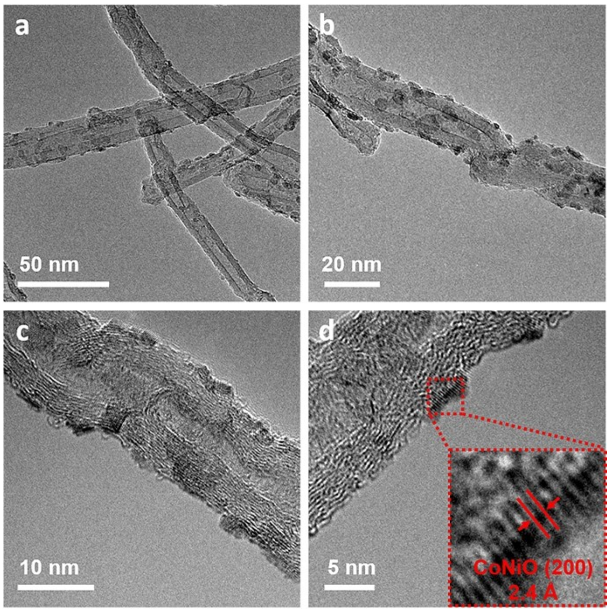

Fig. S10 TEM images of CoNiO$_x$-CNTs. Compared with the TEM images of CNTs in the Fig. S11, it clearly shows that the materials are loading on the CNTs. The enlargement of part (D) shows the (200) crystal plane of the CoNiO. indicating that the materials loading on the CNTs are CoNi oxides.

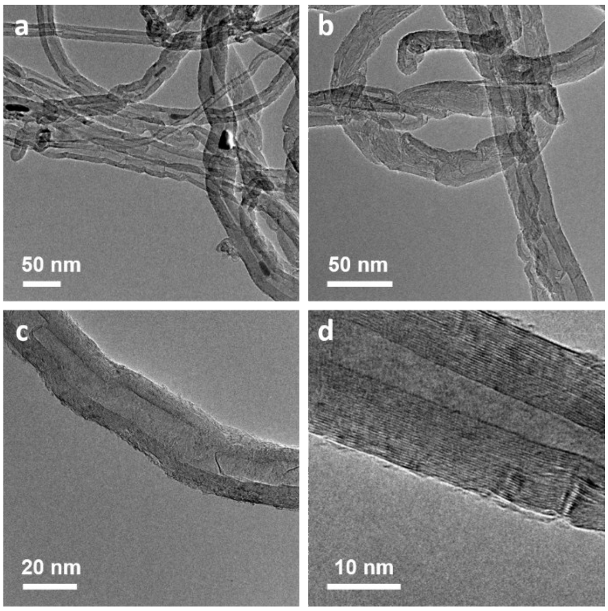

Fig. S11 TEM images of CNTs. It shows that the surface of the CNTs are clean without any loading material.

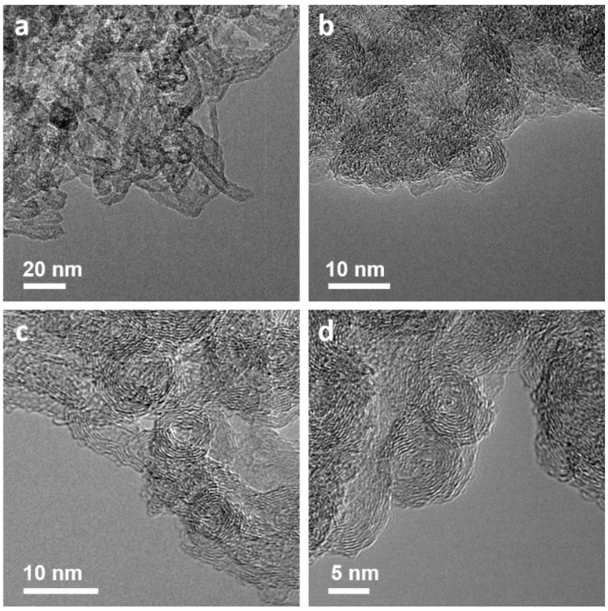

Fig. S12 TEM images of N-Carbon. After the oxidation and acid wash, there is no encapsulated CoNi nanoparticles reserved.

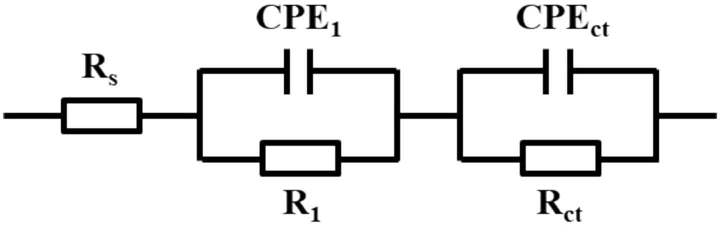

Fig. S13 Equivalent circuit is used for simulating the Nyquist plots in Fig. 2e. The equivalent circuit contains a resistor (R_s), in series with two parallel units of a constant phase element (CPE_1, CPE_{ct}) and a resistor (R_1, R_{ct}), where R_s represents the solution resistance, R_1-CPE_1 is probably related to the interfacial resistance resulting from the electron transport between the catalyst and GCE, R_{ct}-CPE_{ct} reflects the charge transfer resistance at the interface between the catalyst and the electrolyte.

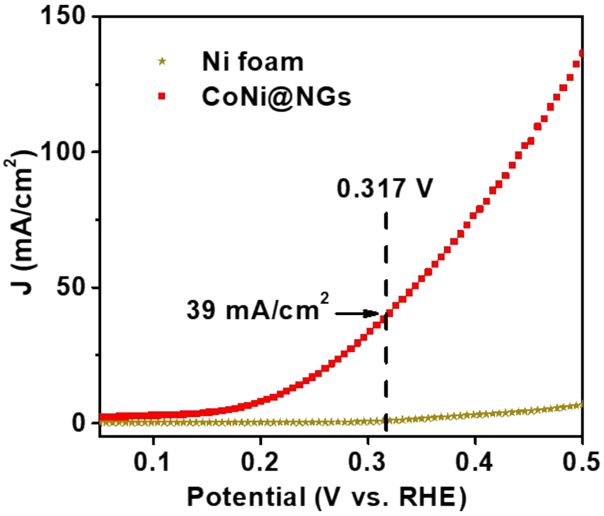

Fig. S14 SOR polarization curves for the working electrode Ni foam dropped CoNi@NGs in comparison with blank Ni foam. The durability of CoNi@NGs was tested for more than 500 h chronoamperometry at 0.317 V (versus RHE). The catalyst was dropped on the Ni foam to form the working electrode. Here, the SOR activity of blank Ni foam substrate was tested at the same condition. Compared with the working electrode dropped CoNi@NGs catalyst, blank Ni foam substrate shows negligible activity in the SOR at 0.317 V.

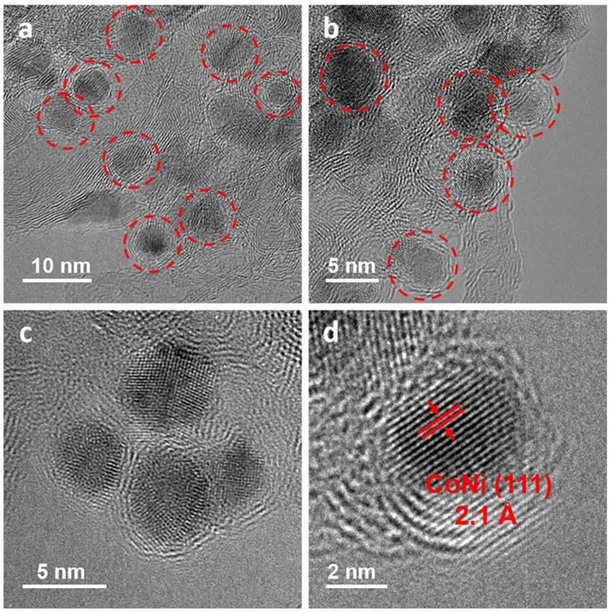

Fig. S15 HRTEM images of the CoNi@NGs sample after 500 h SOR reaction. After 500 h chronoamperometry test, the structure of the graphene shell encapsulating CoNi nanoparticles is still well maintained (red cycle) and the metal nanoparticles in the graphene shell are still metallic state.

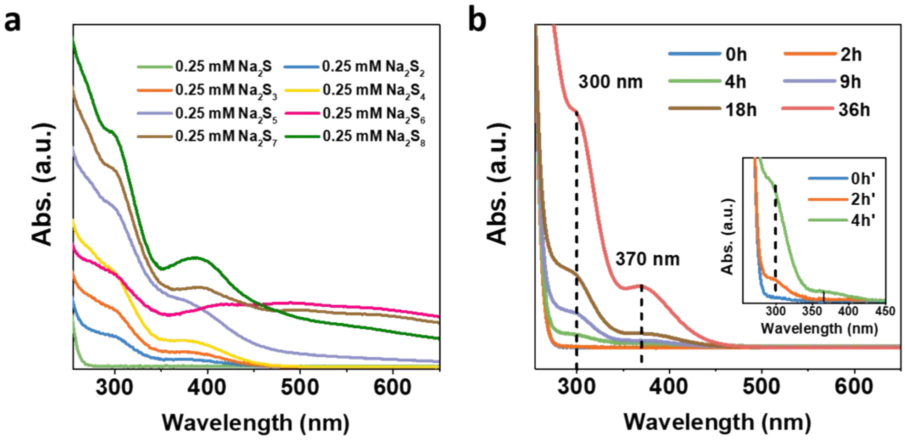

Fig. S16 The species of polysulfide in solution. (a) UV-Vis test for 0.25 mM “standard” polysulfide solution. (b) UV-Vis test for diluent 250 times electrolyte from increasing time of galvanostatic test at 100 mA/cm^2.

The standards in Fig. S16a were prepared by a chemical reaction between stoichiometric amounts of elemental sulfur and Na_2S in the 70 ^oC water bath with magnetic stirring. They were not complete single component solutions. But as the increasing input quantity of S, the color of solutions got darken. Therefore, the UV-Vis test for “standard” polysulfide solutions should have a certain reference value.

From Na_2S_5 to Na_2S_8, with the increasing of polysulfides concentration and chain growth of polysulfides in the solution, it starts to show absorption at larger than 480 nm wavelength in Fig. S16a, which is not existed in the Na_2S_2-Na_2S_4 solutions. Thus, it is considered that the absorption at larger than 450 nm wavelength corresponds to the long-chain of polysulfides. Compared with absorption of UV-Vis test for electrolyte with “standard” polysulfide solutions in the Fig. S16b, it is found that with the increasing of the reaction time, the concentration of polysulfides in the electrolyte become larger and the main groups are short-chain polysulfides (Na_2S_x, x=2-4).

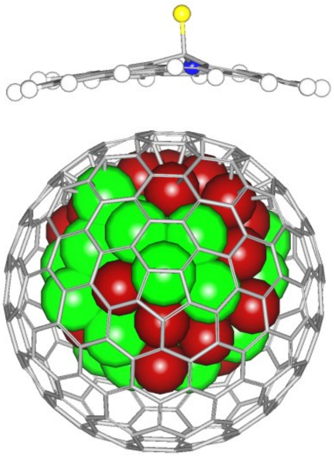

Fig. S17 Schematic illustration of sulfur adsorption on a CoNi alloy encapsulated in two-layer graphene.

In order to gain further insights into the influence of the graphene layer thickness towards the SOR activity, DFT calculations were carried out to examine the sulfur adsorption on two graphene layers encapsulating a CoNi cluster. Then the differences in the free energy of S adsorption [ΔΔG(S*)] for the different layers with and without a CoNi cluster were used to describe the effect of the CoNi cluster on the SOR. As shown in Fig. S18, the metal cluster induces a change in [ΔΔG(S*)] of 2.15 eV when covered by a single graphene layer, whereas with the increase of graphene layer numbers, the promotion of the encapsulated CoNi clusters to the adsorption of sulfur is much weakened. Nevertheless, the promotional effect is still prominent through two layers of graphene and the change amounts to approximately 0.18 eV. This result further indicates that the thinner the graphene shell, the higher the catalytic activity.

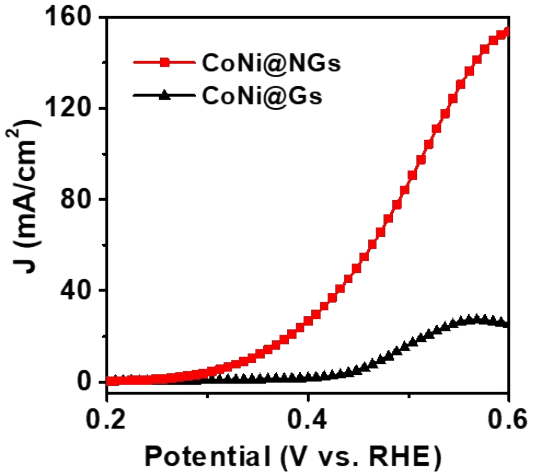

Fig. S18 SOR polarization curves for the samples with CoNi encapsulated in N-doped graphene (CoNi@NGs) and in pure graphene (CoNi@Gs). The experiment results are consistent with the DFT results in Fig. 4d.

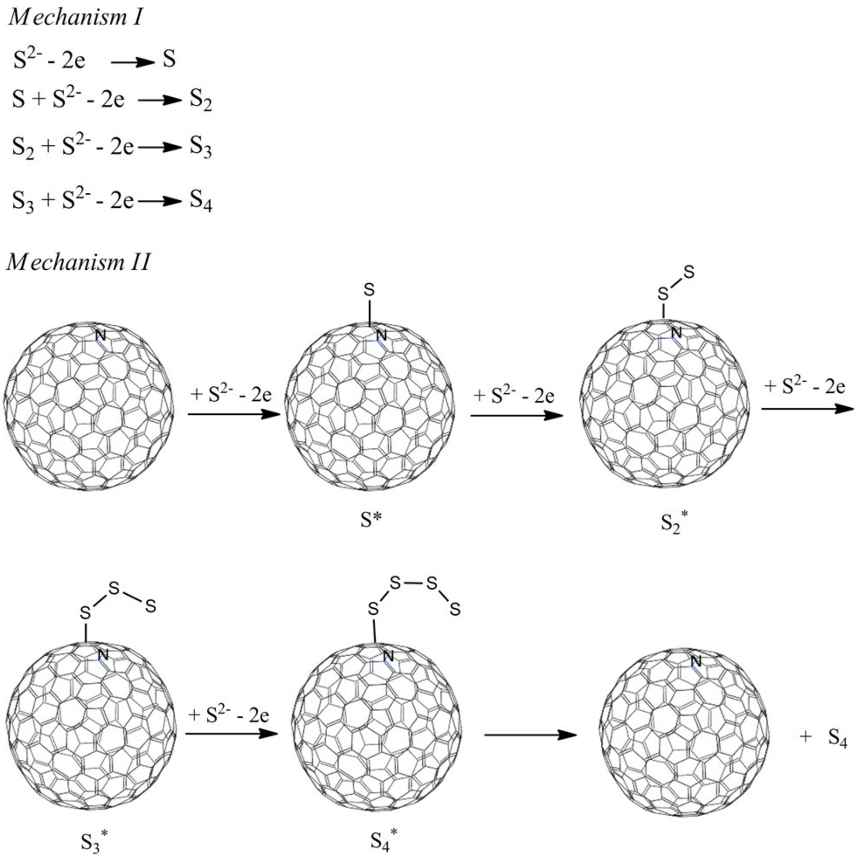

Fig. S19 Schematic representations of the formation of polysulfides (S_x) in the aqueous solution (Mechanism I), on the N-Graphene and CoNi@NGs surface (Mechanism II).

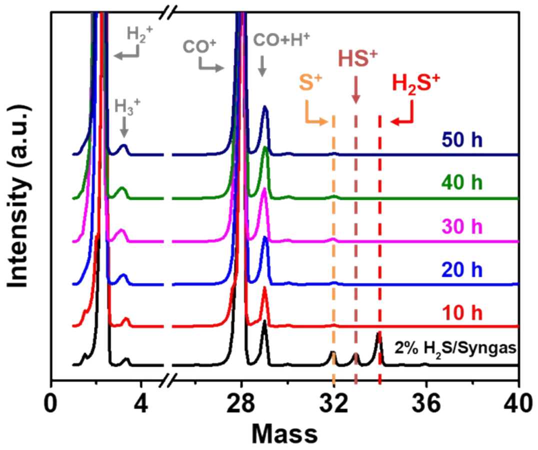

Fig. S20 The composition of the tail gas by real-time mass spectrometry. There was no signal of H_2S in the tail gas, indicating that it was fully absorbed by the alkaline electrolyte.

Table S1. The metal compositions of CoNi@NGs catalysts estimated from ICP measurements.

Sample	Co (wt. %)	Ni (wt. %)
CoNi@NGs-600	10.52	16.85
CoNi@NGs-700	21.51	22.14
CoNi@NGs-800	40.05	44.25

Table S2. The C, H and N element compositions of CoNi@NGs catalysts estimated from Vario EL III measurements.

Sample	C (wt. %)	H (wt. %)	N (wt. %)
CoNi@NGs-600	66.57	0.53	1.86
CoNi@NGs-700	53.01	0.37	1.75
CoNi@NGs-800	10.33	0.33	0.28

Table S3. The comparison of the equilibrium potential of anode reaction for decomposition of H_2S and H_2O.

Reaction Equation	**E_0**
$S^{2-} - 2\ e^- = S$	-0.508 V[8]
$4\ OH^- - 4\ e^- = 2\ H_2O + O_2$	1.23 V

Table S4. Brunner Emmet Teller measurements for CoNi@NGs and reference samples N-Carbon, Co@NGs and Ni@NGs.

Sample	**Specific surface area (m^2/g)**	**Current density (mA/cm^2)**		
		Potential at 0.5 V $_{vs.RHE}$	Potential at 0.55 V $_{vs.RHE}$	Potential at 0.6 V $_{vs.RHE}$
CoNi@NGs	336.23	87	129	153
N-Carbon	419.30	14	36.5	66
Co@NGs	326.76	62	105	144
Ni@NGs	283.18	75	79	40

To figure out the influence of the mass transport limitation for the SOR activity of the materials, Brunner Emmet Teller (BET) measurements were test to characterize the morphology of the catalysts. As shown in the Table S4, the specific surface area of N-Carbon is larger than the CoNi@NGs. The increasing of the specific surface area is due to the removal of the metal cores, which exposes more internal specific surface area of the graphene shell. Although the specific surface area of N-Carbon is larger than

CoNi@NGs, the SOR activity of CoNi@NGs is much higher. It indicated that the influence of metal cores is more important compared with the mass transport limitation.

As for chainmail catalysts with different metal cores, the catalyst with CoNi cores has the largest specific surface area and the best SOR activity (Fig. 4b). By contrast, the Ni@NGs has the smallest specific surface area which reaches the mass transport limitation fast with a sharp decrease at potential above 0.5 V versus RHE. It indicated that for the catalysts with similar structure, increasing the specific surface area would increase the mass transfer which makes the catalyst have a better SOR activity in the higher potential.

Table S5. Current density of SOR for CoNi@NGs compared with the catalysts used in the previous works and related potential catalysts at the potential of 0.3 V, 0.4 V, and 0.5 V (versus RHE). It includes precious materials Pt/C and IrO_2, metallic sulfides, metallic oxides, metal organic compound and carbon materials. As shown in the Table S5, in the same test condition, the graphene encapsulating metal catalysts developed in this work displayed the superior activity than any of the contrast catalysts mentioned in the previous works.

Sample	**Current density (mA/cm^2) at different potential**			**Reference**
	0.3 V	**0.4 V**	**0.5 V**	
CoNi@NGs	4.09	26.55	87.44	This work

Co@NGs	1.97	11.07	61.76	This work
Ni@NGs	3.83	27.05	75.36	This work
40% Pt/C	3.31	14.73	46.88	[9]
IrO_2	1.80	6.57	22.06	[10]
Raney Ni	0.50	1.39	3.65	[9]
CoS	1.46	2.14	3.04	[9, 11, 12]
NiS	0.43	0.71	1.38	[13]
CuS	0.88	1.19	1.59	[11]
MoS_2	0.48	0.70	0.93	[14]
Co_3O_4	0.65	0.97	1.83	[15]
NiO	0.42	0.50	0.72	[15]
Fe_3O_4	0.37	0.46	0.75	[15]
CoPc	0.37	1.00	1.92	[16]
NiPc	0.30	0.38	0.52	[16]
CuPc	0.32	0.40	0.59	[16]
FePc	0.80	5.61	7.90	[16]
Graphene	0.38	2.77	23.13	[9]
Graphite	0.19	0.33	0.78	[9]
CNTs	0.31	0.92	4.02	[17]
Super P	0.50	0.69	1.65	[18]
XC-72	0.18	0.42	4.85	[9, 12]

Table S6. Electrochemical impedance parameters obtained via simulating the Nyquist plots to the equivalent circuit model in Fig. S13.

Sample	**R_s** **[Ω]**	**CPE_1** **[$S*s^{n}{}_1$]**	**R_1** **[Ω]**	**CPE_{ct}** **[$S*s^{n}{}_2$]**	**R_{ct}** **[Ω]**	**n_1**	**n_2**
CoNi@NGs	3.579	0.002462	11.55	0.1345	1.441	0.8252	0.8342
CoNiO$_x$-CNTs	3.62	0.002468	33.79	0.03927	14.09	0.7336	0.9807
40% Pt/C	3.606	0.002542	4.897	0.01123	16.5	1	0.671
CNTs	3.692	0.000219	150.3	0.003117	582.9	0.9408	0.6953

Table S7. Adsorption free energy of S ($\Delta G(S^*)$) (in eV) for various models.

Structures	$\Delta G(S^*)$
CoNi@NGs	-0.29
Ni@NGs	0.66
Co@NGs	0.84
N-Graphene	1.87
Carbon	2.02
CoNi	-1.76

Table S8. The pH value of electrolyte in the anodic and cathodic cell in the 50 h demo test of removal H_2S from syngas.

Time (h)	Anode (SOR)	Cathode (HER)
0	13.93	13.93
25	13.83	13.91
50	13.81	13.88

REFERENCES

1. G. Kresse and J. Furthmuller, *Comput. Mater. Sci.*, 1996, **6**, 15-50.
2. G. Kresse and J. Furthmuller, *Phys. Rev. B*, 1996, **54**, 11169-11186.
3. G. Kresse and J. Hafner, *Phys. Rev. B*, 1993, **47**, 558-561.
4. G. Kresse and J. Hafner, *Phys. Rev. B*, 1994, **49**, 14251-14269.
5. P. E. Blochl, *Phys. Rev. B*, 1994, **50**, 17953-17979.
6. G. Kresse and D. Joubert, *Phys. Rev. B*, 1999, **59**, 1758-1775.
7. J. P. Perdew, K. Burke and M. Ernzerhof, *Phys. Rev. Lett.*, 1996, **77**, 3865-3868.
8. Z. Mao, A. Anani, R. E. White, S. Srinivasan and A. J. Appleby, *J. Electrochem. Soc.*, 1991, **138**, 1299-1303.
9. K. Petrov and S. Srinivasan, *Int. J. Hydrogen Energy*, 1996, **21**, 163-169.
10. B. Miller and A. Chen, *Electrochim. Acta*, 2005, **50**, 2203-2212.
11. G. Hodes, J. Manassen and D. Cahen, *J. Electrochem. Soc.*, 1980, **127**, 544-549.
12. L. Su, A. F. Badel, C. Cao, J. J. Hinricher and F. R. Brushett, *Industrial & Engineering Chemistry Research*, 2017, **56**, 9783-9792.
13. J. Hao, W. Yang, J. Hou, B. Mao, Z. Huang and W. Shi, *J. Mater. Chem. A*, 2017, **5**, 17811-17816.
14. A. E. Sanlı, A. Aytaç and M. Mat, *International Journal of Hydrogen Energy*, 2014, **39**, 9221-9229.
15. S. Jung, C. C. L. McCrory, I. M. Ferrer, J. C. Peters and T. F. Jaramillo, *J. Mater. Chem. A*, 2016, **4**, 3068-3076.
16. Š. Komorsky-Lovrić, M. Lovrić and F. J. M. A. Scholz, 1997, **127**, 95-99.
17. B. G. Ateya, F. M. Al-Kharafi, R. M. Abdallah and A. S. Al-Azab, *Journal of Applied Electrochemistry*, 2005, **35**, 297-303.
18. Z. Ma, Z. Li, K. Hu, D. Liu, J. Huo and S. Wang, *J. Power Sources*, 2016, **325**, 71-78.